Scientific Journals
of the Maritime University of Szczecin

Zeszyty Naukowe
Akademii Morskiej w Szczecinie

2020, 62 (134), 124–135
ISSN 1733-8670 (Printed)
ISSN 2392-0378 (Online)
DOI: 10.17402/427

Received: 24.02.2019
Accepted: 12.05.2020
Published: 29.06.2020

Experimental and numerical determination of the hydrodynamic coefficients of an autonomous underwater vehicle

Abdollah Sakaki[1]✉, Mohsen Sadeghian Kerdabadi[2]

Amirkabir University of Technology, Tehran, Iran
e-mail: [1] a.sakaki@aut.ac.ir, [2] sadeghian2@aut.ac.ir
✉ corresponding author

Key words: Reynolds averaged Navier–Stokes, computational fluid dynamics, linear coefficients, non-linear coefficients, underwater vehicle

Abstract
Computational fluid dynamics (CFD) has progressed rapidly in the past fifty years and is now used in many industrial fields, such as air, space, and marine engineering. CFD has an irreplaceable role in marine design and scientific research, and its applications within this field continue to grow with the development of computers. CFD is used to quickly and inexpensively simulate fluid behaviour using the Reynolds Averaged Navier–Stokes (RANS) equations to calculate hydrodynamic coefficients, which are needed in manoeuvrability studies of underwater vehicles (UWV). Here, these computations are performed for six geometrical shapes that represent typical autonomous underwater vehicles (AUVs) currently in use. Resistance test simulations at up to 20° drift angles were conducted for AUVs with different length-to-diameter ratios. The results were compared with the experimental data and current quasi-experimental relationships, which suggested that the CFD predictions were adequately precise and accurate. These predictions indicated that there was a non-linear relationship between forces and moments and the lateral speed. Moreover, both linear and non-linear hydrodynamic coefficients were calculated.

Introduction

An analysis system based on CFD simulations has been developed to calculate the hydrodynamic coefficients and hydrodynamic forces acting on UWVs. Numerical approaches have improved to a level of accuracy that allows them to be applied for practical marine vehicle resistance and industrial propulsion computations. Recently, CFD has also been used to determine hydrodynamic coefficients, which are required to evaluate the manoeuvring characteristics of underwater marine vehicles. Traditionally, the hydrodynamic coefficients of UWVs have been predicted using one of three methods: potential flow methods, semi-empirical methods, and experimental model tests. The last can be further divided into oblique towing tests, rotating arm experiments, and planar motion mechanism (PMM) tests (Kim et al., 2007; Obreja et al., 2010; Li & Duan, 2011; Fan et al., 2012; Pan, Zhang & Zhou, 2012).

UWVs can be classified as either manned or unmanned systems. Manned systems can be categorized into two sub-classes: military submarines and non-military submersibles, such as those operated to support underwater investigations and assessments. Unmanned submersibles fall into several different sub-classes. The simplest and most easily described are submersibles that are towed behind a ship, and the second type is called a remotely operated vehicle (ROV), which is a tethered vehicle. The third type of unmanned submersible is an unmanned untethered vehicle (UUV), which contains its own onboard power but is controlled by a remote operator via

a communications link. An autonomous underwater vehicle (AUV) is an undersea system with its own power that controls itself while performing a pre-defined task. A further distinction between AUVs and UUVs is that AUVs require no communication during their mission, whereas UUVs require some level of communication to complete their mission (Blidberg, 2001).

AUVs are automatic, intelligent vehicles that can cover a given path and undertake a variety of activities, such as land surveying, identification, and mine detection, over a vast area without using cables. These ocean vehicles must be capable of rapid decision-making to cope with different conditions; therefore, their manoeuvrability and controllability are of great importance. In recent years, there have been many efforts to develop these vehicles. To design an AUV, its manoeuvrability and controllability must be accurately calculated using mathematical models. The current mathematical models provide hydrodynamic forces and moments, which are defined as hydrodynamic coefficients; therefore, accurately calculating these coefficients is essential for simulating an AUV's performance.

Hydrodynamic coefficients are divided into three types: linear damping coefficients, linear inertia coefficients, and non-linear damping coefficients. Among these, temporal linear coefficients, in which an AUV moves in a steady flow, affect the manoeuvrability, while in unsteady flow, linear inertia coefficients and non-linear coefficients should be taken into consideration. These coefficients are usually determined by conducting system identification tests or experimental formulas, whose precision depends on different conditions, such as the hull geometry and operating conditions. Most of these methods can only calculate linear coefficients, and there is currently no experimental relationship for calculating the hydrodynamic coefficients of an AUV, and the application of ship or submarine-related relationships for an AUV produces many errors. Temporal system identification is useful when adequate experimental data are available to design a suitable mathematical model. Another problem is that during the initial design, manoeuvrability is not applicable. Although PPM tests are one of the most common methods for calculating coefficients, they are expensive and require long calculation times with many experimental errors.

Several methods are used to obtain hydrodynamic coefficients, including theoretical approaches, semi-empirical formulas, captive model tests, and CFD. As computers have developed, CFD has become increasingly used in the marine industry during the design stage. Numerical methods are so precise and accurate that they are used in resistance and thrust calculations. In recent years, the CFD method has also been used to calculate the hydrodynamic coefficients for manoeuvrability predictions (Ferziger, Peric & Leonard, 1997; Tyagi & Sen, 2006; Williams et al., 2006).

Reynolds Averaged Navier–Stokes (RANS) equations were first used to solve maritime problems more than 20 years ago, but they produced unsatisfactory results (Wilson, Paterson & Stern, 1998; Gentaz et al., 1999). With increased computing capacities and recent progress in RANS models, great advances have been made in this field, and CFD has become a crucial tool for various aspects of UWV hydrodynamics for both research and design. One of the most recent and important applications of CFD in the marine industry is its use to compute the hydrodynamic coefficients of marine vehicles during captive model simulations. For example, Sarkar developed a new computationally efficient technique to simulate 2-D flow over axisymmetric AUVs using the PHOENICS CFD package (Sarkar, Sayer & Fraser, 1997). Fluent CFD code was used to obtain the hydrodynamic coefficients of 3-D fins and an AUV, as well as to compute the linear and nonlinear hydrodynamic coefficients of a SUBOFF submarine in an unrestricted fluid flow (Ray, Singh & Seshadri, 2009; Nazir, Su & Wang, 2010). The transverse hydrodynamic coefficients of an AUV were computed using a commercial CFD package (Tyagi & Sen, 2006), and the hydrodynamic forces and moments acting on an AUV due to control surface deflection were investigated using ANSYS Fluent software (Dantas & de Barros, 2013). CFD was used to construct a platform for AUV hull shape optimization, but only primitive particle swarm optimization (PSO) and multi-island genetic algorithm (MIGA) methods were compared (Gao et al., 2016).

In this study, a new method is proposed for simulating hydrodynamic tests using a CFD software named CD-adapco, which discretizes Navier–Stokes equations through the finite volume method with respect to the boundary and initial conditions. The software was used to solve the final equation system, which allowed the hydrodynamic coefficients used in the mathematical manoeuvre model to be calculated. This computational model was highly suitable, cost-effective, and flexible to use. Six models with different length-to-diameter ratios and different speeds were calculated and compared.

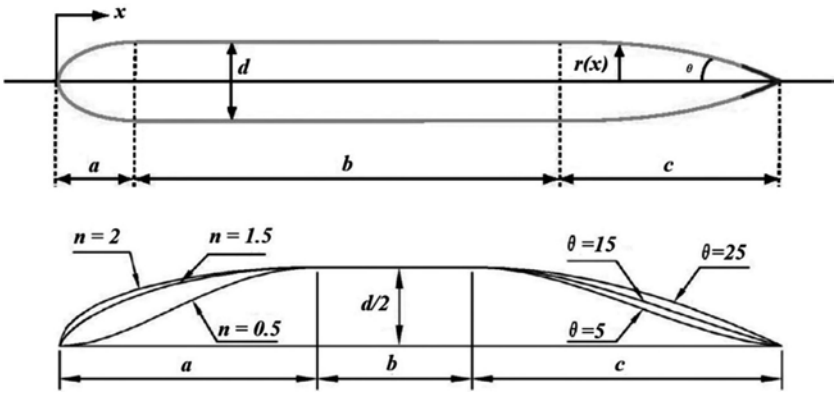

Figure 1. Illustration of Myring AUV (Gao et al., 2016)

Description of the model

A Myring-type body was used to parameterize the AUV hull shapes and was chosen due to its streamlined characteristics. The Myring AUV class has already applied in aircraft fuselage and other AUVs such as Maya and Remus, Pirajuba, and Guanay II. A Myring-type AUV has three distinct parts: the nose section, the middle body cylindrical section, and the tail section. The nose and the tail sections are defined by a semi-elliptical radius distribution along the main axis, as given by the following equations (Myring, 1976):

$$\text{Bow} \rightarrow r(x) = \frac{1}{2} d \left[1 - \left(\frac{x-a}{a} \right)^2 \right]^{\frac{1}{n}}$$

$$\text{Stern} \rightarrow r(x) = \frac{1}{2} d - \left(\frac{3d}{2c^2} - \frac{\tan\theta}{c} \right) (x-a-b)^2 + \left(\frac{d}{c^3} - \frac{\tan\theta}{c^2} \right) (x-a-b)^3 \quad (1)$$

where x is the axial distance to the nose tip; a, b, and c are the lengths of the nose, middle and tail, respectively; d is the middle hull diameter; n is the index of the nose shape; and θ is semi-angle of the tail. The section of the Myring AUV and Model dimensions are shown in Figure 1 and Table 1.

Table 1. Model Dimensions

	Parameter	Value	Unit
1	Hull maximum diameter (d)	0.234	m
2	Tail length (c)	0.279	m
3	Nose length (a)	0.217	m
4	Middle body length (b)	1.246	m
5	Tail semi-angle (θ)	25	deg
6	Myring body parameter	2	–

Case study

Experimental setup

In this study, six AUVs were used to simulate hydrodynamic tests. The model with a 7.5

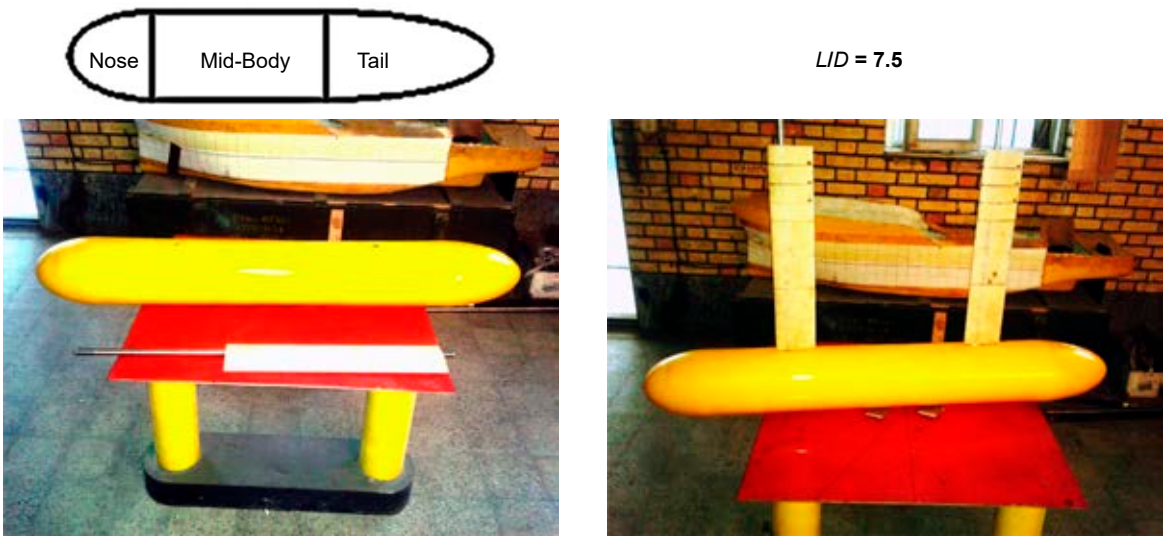

Figure 2. The model tested in the towing tank of Isfahan University of Technology

length-to-diameter ratio was designed and manufactured in the towing tank of Isfahan University of Technology (Figures 2 and 3). Experiments were also conducted in this towing tank (108×3×2.2 m), whose basin was equipped with a trolley that could provide a carriage speed up to 6 m/s with ±0.02 m/s accuracy. For force measurements, a 3-DOF dynamometer was installed with 100 N load cells that were calibrated using calibration weights with 1% uncertainty. The experimental plan included performing straight-ahead resistance runs at various forward speeds (U = 0.5, 0.75, 1, 1.5, 2, 2.5, 3, and 4 m/s).

Figure 3. Experimental setup

Other models were designed by Oceanic Consulting Corporation (OCC) in Canada in 2005 and were tested in 90-meter long and 12-meter wide NTC-IOT towing tanks (Williams et al., 2006; Azarsina, Williams & Issac, 2008; Azarsina & Williams, 2010). The length-to-diameter ratio of this model was 8.5, and different models with the same diameter and different lengths were rebuilt and tested for improvement. A schematic view of the models is shown in Figure 4. Table 2 explains the six tested models.

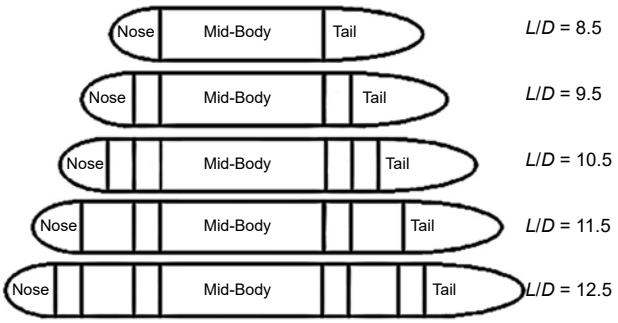

Figure 4. Schematic of the five configurations tested in OCC (Williams et al., 2006)

Table 2. Details of the six tested models

L/D	LOA mm	Moment centre (nose) mm	LCB mm	Ratio MC to LOA	Ratio LCB to LOA
7.5	1521	634	714	0.418	0.471
8.5	1724	736	815	0.427	0.473
9.5	1927	838	915	0.435	0.475
10.5	2130	940	1017	0.441	0.477
11.5	2333	1041	1118	0.446	0.479
12.5	2536	1143	1220	0.451	0.481

Governing equations

Maneuvering equation

A body coordinate system *o-xyz* (Figure 5) was defined to calculate the manoeuvring equations, such that *oz* is the vertical axis and positive downward; *ox* is the longitudinal axis and positive toward the nose of the vehicle; and *oy* is the transverse axis and positive toward the starboard side of a vehicle. If it is assumed that the body is moving in the horizontal plane *o-xy*, the origin *o* coincides with the centre of mass, and the coordinate system coincides with the principal axes of inertia. The motion equations may be given as follows (Eq. (2)–(4)) for an AUV in the body coordinate system *o-xyz* that is moving relative to the inertial coordinate system *O-XYZ*.

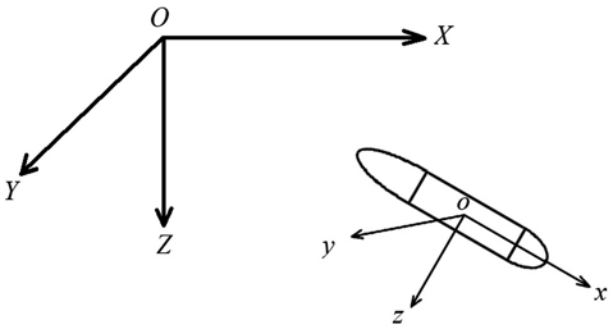

Figure 5. Coordinate system (*O-XYZ* is earth fixed coordinate and *o-xyz* is the body-fixed coordinate system)

$$m\left(\dot{u}-rv\right)=X \tag{2}$$

$$m\left(\dot{v}+ru\right)=Y \tag{3}$$

$$I_z\dot{r}=N \tag{4}$$

The first equation is the surge motion equation, and the second and third equations are sway and yaw motion equations, respectively. X and Y are external forces along the x and y-axis, respectively, and N is the external moment about the z-axis; m is the mass

of the body; I_z is the moment of inertia of the body about the z-axis; u is body velocity along the x-direction; and v is the velocity of the body along the y-direction; $\dot{u}$ and $\dot{v}$ are the acceleration of the body along the x and y directions, respectively; and r and $\dot{r}$ are the angular velocity and acceleration around the z-axis of the body.

The nonlinear external forces X and Y and moment N may be written as follows (Eq. (5)–(7)) according to the Abkowitz model based on the quasi-steady-state assumption, which states that the forces at any instant depend on the motion parameters that define the instantaneous motion of the vessel. The body is moving in a self-propulsion point, and the control surface is in the neutral condition.

$$X = X_{\dot{u}}\dot{u} + X_u u + X_{uu}u^2 + X_{uuu}u^3 + X_{vv}v^2 + \\ + X_{rr}r^2 + X_{vr}vr + X_{vvu}v^2u + X_{rru}r^2u + X_{uvr}uvr \quad (5)$$

$$Y = Y_r r + Y_v v + Y_{\dot{r}}\dot{r} + Y_{\dot{v}}\dot{v} + Y_{rrr}r^3 + Y_{vvv}v^3 + Y_{vrr}vr^2 + \\ + Y_{vvr}v^2r + Y_{vu}vu + Y_{ru}ru + Y_{vuu}vu^2 + Y_{ruu}ru^2 \quad (6)$$

$$N = N_r r + N_v v + N_{\dot{r}}\dot{r} + N_{\dot{v}}\dot{v} + N_{rrr}r^3 + \\ + N_{vvv}v^3 + N_{vrr}vr^2 + N_{vvr}v^2r + N_{vu}vu + \\ + N_{ru}ru + N_{vuu}vu^2 + N_{ruu}ru^2 \quad (7)$$

The coefficients on the right-hand side of the equations are the hydrodynamic derivatives or manoeuvring coefficients. Among the several available methods for determining hydrodynamic coefficients, the PMM test is a single system that can explicitly provide all damping and added mass coefficients required in the equations of motion. In this paper, the OTT is simulated using CFD to obtain the linear parameters such as Y_v and N_v and the nonlinear parameters such as X_{vv}, Y_{vvv}, and N_{vvv}.

Fluid flow modelling

The unsteady viscous flow around a marine vehicle is governed by the Navier–Stokes equations, which can be applied to both laminar and turbulent flow, but a very fine meshing is necessary to capture all the turbulence effects in the turbulent flow regime. RANS equations can also be used to model the turbulent flow. They are obtained based on statistical tools known as Reynolds decomposition, where the flow parameters are decomposed into time-averaged and fluctuation components, i.e. $u = \overline{u} + u'$, $p = \overline{p} + p'$ where $\overline{u}$ and $\overline{p}$ are the time-averaged, and u', p' are the fluctuation velocity and pressure, respectively. The RANS equations are given as follows for incompressible flow:

$$\frac{\partial\left(\rho\overline{u}_i\right)}{\partial x_i} = 0 \quad (8)$$

$$\frac{\partial\left(\rho\overline{u}_i\right)}{\partial t} + \frac{\partial}{\partial x_j}\left(\rho\overline{u}_i\overline{u}_j + \rho\overline{u_i'u_j'}\right) = \\ = -\frac{\partial\overline{p}}{\partial x_i} + \rho g_i + \frac{\partial}{\partial x_j}\left[\mu\left(\frac{\partial\overline{u}_i}{\partial x_j} + \frac{\partial\overline{u}_j}{\partial x_i}\right)\right] \quad (9)$$

where ρ is the fluid density; g_i is the x, y, and z components of gravitational acceleration; μ is the fluid dynamic viscosity; and $\rho\overline{u_i'u_j'}$ is the Reynolds stress tensor components. The Reynolds stress tensor components are estimated by turbulence models, which are approximations of the physical phenomena of turbulence. ρ is the density of the fluid, and the Reynolds stress tensor is defined as:

$$\rho\,\overline{u}_i'\,\overline{u}_j' = \begin{bmatrix} \rho\overline{u}_1'^2 & \rho\overline{u}_1'\,\overline{u}_2' & \rho\overline{u}_1'\,\overline{u}_3' \\ \rho\overline{u}_2'\,\overline{u}_1' & \rho\overline{u}_2'^2 & \rho\overline{u}_2'\,\overline{u}_3' \\ \rho\overline{u}_3'\,\overline{u}_1' & \rho\overline{u}_3'\,\overline{u}_2' & \rho\overline{u}_3'^2 \end{bmatrix} \quad (10)$$

Turbulence Model:

For the turbulence model, the k-ε model and Reynolds stress transformation model were used. The k-ε model is one of the most common turbulence models used for aerodynamic and hydrodynamic problems. After comparing the available models, this model was selected for the final simulations and was defined with respect to two functions for parameters k and ε as:

$$\frac{\partial\rho k}{\partial t} + \nabla\left(\rho\overline{U}k\right) = \nabla\left[\left(\mu + \frac{\mu_t}{\sigma_k}\right)\nabla k\right] + P_k - \rho\varepsilon \quad (11)$$

$$\frac{\partial\rho\varepsilon}{\partial t} + \nabla\left(\rho\overline{U}\varepsilon\right) = \\ = \nabla\left[\left(\mu + \frac{\mu_t}{\sigma_k}\right)\nabla\varepsilon\right] + \frac{\varepsilon}{k}\left(C_{\varepsilon 1}P_k - C_{\varepsilon 2}\rho\varepsilon\right) \quad (12)$$

and then:

$$P_k = \mu_t\nabla\overline{U}\left(\nabla\overline{U} + \nabla\overline{U}^T\right) - \frac{2}{3}\nabla\overline{U}\left(3\mu_t\nabla\overline{U} + \rho k\right) \quad (13)$$

$$\mu_t = C_\mu\rho\frac{k^2}{\varepsilon} \quad (14)$$

Boundary conditions

The appropriate boundary conditions on the fluid domain boundaries and an AUV's hull must be used to create a well-posed system of equations. The domain boundaries were split into patches as shown in Figure 6. The boundary conditions were chosen to avoid backflow and lateral wall effects. There are two boundary conditions for the body surface: the kinematic condition of no flow through the surface, and a no-slip condition on the tangential velocity. These are applied on the instantaneous wetted surface of the AUV. For other boundaries, the symmetry plane condition is a Neumann condition which means that pressure, tangential velocities, and turbulence quantities have a zero gradient normal to the surface; however, for the normal velocity component, a Dirichlet condition is applied.

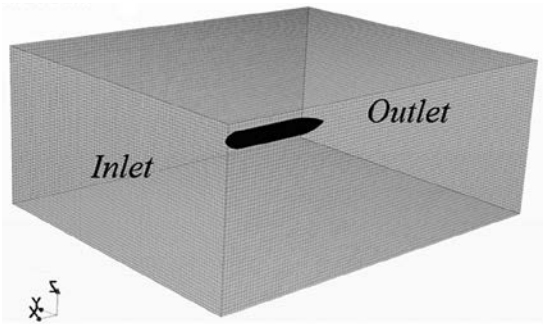

Figure 6. Illustration of the computational domain

The finite volume method (FVM) is commonly used to computationally solve RANS equations in the computational domain by discretizing into finite control volumes in which the discretized RANS equations are solved. The domain dimensions are selected to be sufficiently large to prevent backflow at high drift angles. The distance from the inlet boundary from the AUV nose tip is considered 1*L*, the distance of outlet boundary from the AUV tail is considered 2*L,* and the side boundaries are located at 0.5*L* (Figures 6 and 7).

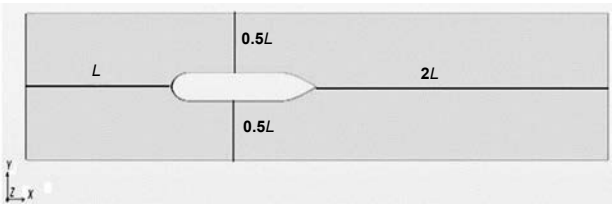

Figure 7. Schematic of the computational domain

To solve the Navier–Stokes time-averaging equations, the boundary conditions of walls and the hull wall were fulfilled, as shown in Figure 4, as:

1. Flow input (right boundary): Flow enters with a steady, specific speed.
2. Flow output (left boundary): Flow exits with a steady pressure distribution.
3. Symmetry (other boundaries): These boundaries are defined by a symmetry condition to prevent wall effects and fulfil the limited water condition.
4. Wall (surface of the body): The surface of the body is defined as an impenetrable wall.

Mesh generation

There are different structured and unstructured meshing strategies for solving different problems. Simulations are conducted on unstructured trimmed meshes, while a trimmer meshing strategy is proficient for generating a high-quality mesh with the lowest grid skewness. The overall view of the mesh in the computational domain and around the AUV is displayed in Figures 8 and 9, respectively. The mesh distribution in the simulation range near the initial model is shown in Figure 10.

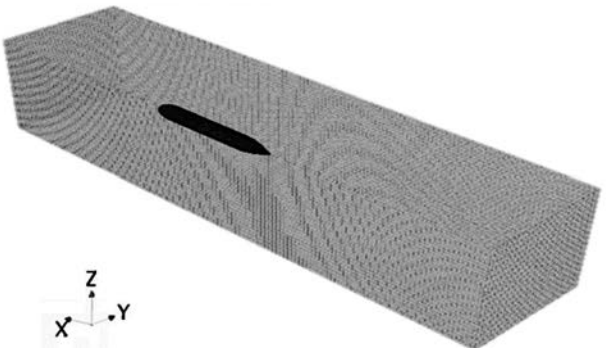

Figure 8. Computational domain

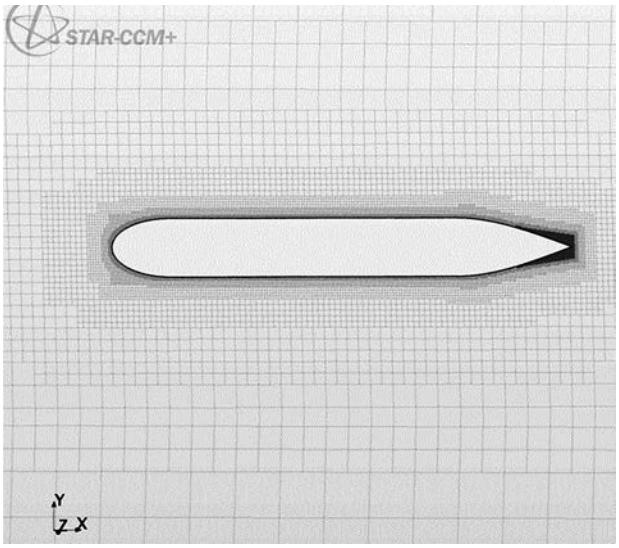

Figure 9. Mesh around the hull

Figure 10. Mesh distribution in the simulation range near the initial model

Prism layer refinement was applied to the hull to improve the accuracy of the solution in the boundary layer region. The turbulent flow inside the boundary layer was approximated by wall functions. A high $y+$ wall treatment based on equilibrium turbulent boundary layer theory was used as the wall function. The mean value of $y+$ on the hull surface was around 30, indicating good refinement of the prism layer. The distribution of $y+$ for the fine mesh on the hull is shown in Figure 11.

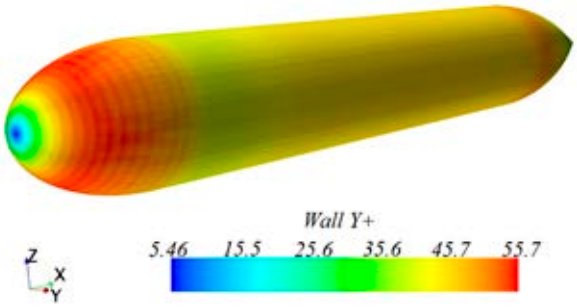

Figure 11. Distribution of $y+$ around the hull

Grid convergence

Mesh sensitivity examination is the most straightforward and consistent technique for determining the order of discretization errors in numerical simulations. In other words, numerical results can be considered precise and valid if their solution is independent of the grid. A mesh sensitivity study involves implementing solutions on the CFD model, with sequentially refines grids with reduced mesh sizes until the variables become independent of the mesh size. Three different mesh sizes with a constant grid refinement factor ($r = h_2/h_1 = h_3/h_2 = 1.65$) were been chosen, in which h_i is a characteristic dimension of the model, for example, the AUV length that is used to measure the mesh discretization. To prevent errors arising from extrapolation, based on experience, it is recommended that $r > 1.3$. The corresponding solutions for these cases are designated s_1 through s_3.

The mesh study for simulations was examined for the pure model with zero drift angle at $U = 2$ m/s, and the corresponding forces and moment of each mesh were calculated. Mesh numbers, forces, and moments are shown in Table 3.

Table 3. Axial force for different grids

Number of grids	Type of mesh	F_x
1,456,325	Coarse	–8.236
2,529,846	Medium	–7.735
4,077,078	Fine	–7.542

The convergence ratio is defined as follows:

$$R = \frac{\varepsilon_{21}}{\varepsilon_{32}} \tag{15}$$

where $\varepsilon_{21} = s_2 - s_1$ is the difference between the solutions of fine and medium grids, and $\varepsilon_{32} = s_3 - s_2$ is the difference between the solutions of the medium and coarse grids.

The possible convergence situations are:
$R > 1 \Rightarrow$ Grid divergence,
$R < 0 \Rightarrow$ Oscillatory convergence,
$0 < R < 1 \Rightarrow$ Monotonic grid convergence.

If grid convergence occurs, Richardson extrapolation (also called h^2 extrapolation) is used to estimate the convergence rate. The fractional difference between solutions is defined as $e_{ij} = (s_j - s_i)/s_i$; hence, the order of the discretization is estimated as follows:

$$p = \frac{\log(e_{32}/e_{21})}{\log(r)} \tag{16}$$

After that, the grid convergence index (GCI) is defined as:

$$\mathrm{GCI}_{ij} = F_S \frac{|e_{ij}|}{r^p - 1} \tag{17}$$

In this equation, F_s is a safety factor that Roache (Roache, 1997) recommended for convergence studied with a minimum of three grids ($F_s = 1.25$). GCI indicates the difference between the calculated and exact value and is also a measure of solution changes upon additional grid refinement. A small GCI value indicates that the solution is in the exact value range.

The computed convergence ratio, order of discretization, and GCI are shown in Table 4. The theoretical value for convergence is $p = 2$, and the difference is due to the orthogonal grid, problem nonlinearities, turbulence modelling, etc.

Table 4. Estimated convergence ratio, the order of discretization, and GCI

	F_x
R	0.206
p	2.930
$\mathrm{GCI}_{\mathrm{fine}}$	0.009

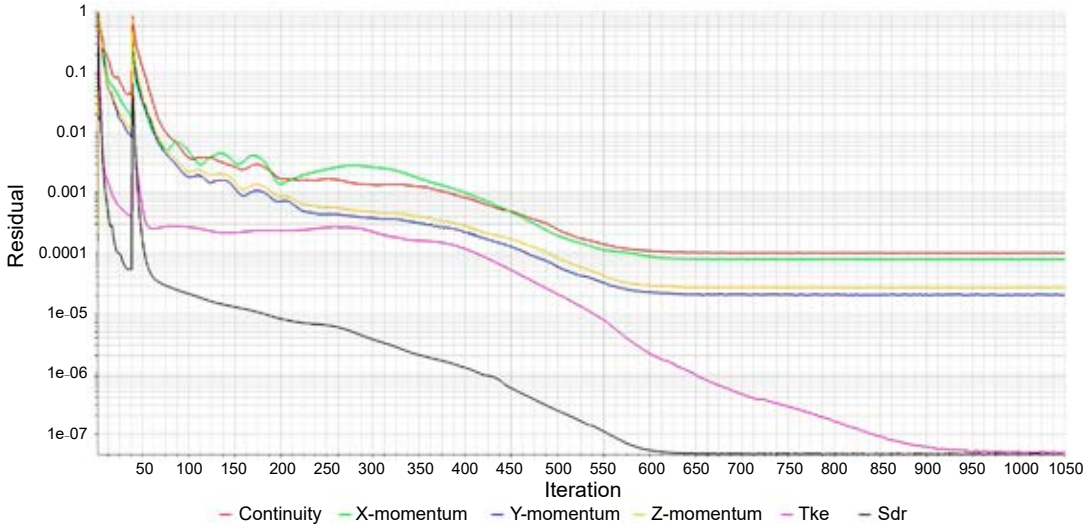

Figure 12. Residual of continuity, momentum, and turbulence parameters

Computational fluid dynamic simulations

The fluid flow around the model was simulated with and without a drift angle with respect to the fluid flow direction. For the case without a drift angle, the resistance can be obtained using resistance simulations. In the case with a drift angle (the static drift angle), the damping coefficients dependent on the lateral velocity can be obtained. All computations were performed with a SIMPLE algorithm for pressure-velocity coupling. The second-order upwind scheme was applied for the advection term in the momentum equation. The most common method for checking the convergence of the simulation results is to investigate the residual of each solved variable. In Figure 12, an illustrated of residual is shown, which indicated good convergence.

Resistance simulation

The resistance test was simulated for a bare hull at U = 0.5–4 m/s with an increment of 0.5 m/s to investigate the axial force on an AUV. As noted, the straight-ahead resistance experiment was performed at U = 0.5, 0.75, 1, 1.5, 2, 2.5, 3, and 4 m/s, and the resistance of the bare hull was estimated based on the empirical equation. In this method, the resistance was predicted using:

$$R_{\text{Barehull}} = \frac{1}{2}\rho A V^2 C_t \tag{18}$$

where A is the wetted surface area, V is the velocity, ρ is the water density, and C_t is the total drag coefficient of the hull that is calculated as follows:

$$C_t = C_f\left[1 + 1.5\left(\frac{d}{l}\right)^{1.5} + 7\left(\frac{d}{l}\right)^{3}\right] \tag{19}$$

where C_f is the frictional resistance coefficient that is calculated according to the ITTC 1957 friction formula:

$$C_f = \frac{0.075}{(\log \text{Re} - 2)^2} \tag{20}$$

where Re is the Reynolds number. The results obtained for bare hull resistance are shown in Figure 13. A comparison of the experimental, numerical, and empirical results is presented in Figure 13, which shows that the CFD solution provided a good prediction of the experimental and empirical results for different velocities.

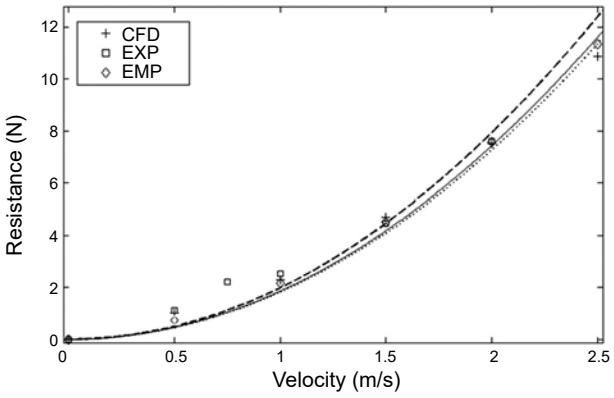

Figure 13. Comparison of computed, experimental, and empirical resistance vs. velocity

Results

Simulations were conducted on six symmetric bare hulls. The initial bare hull is shown in Figures

1 and 4, with a length-to-diameter ratio of 7.5. Other models with the same diameter and 8.5, 9.5, 10.5, 11.5, and 12.5 length-to-diameter ratios were designed for conditions in which more space for equipment or increased battery capacity was needed; therefore, a set of simulations was conducted using different speeds for these models.

Resistance tests

Resistance simulations were conducted for 6 hulls at speeds of 1, 2, 3, and 4 m/s. All simulations were conducted in the absence of an angle of attack. An example of the speed distribution around the hull model is shown in Figure 14.

The longitudinal force in each simulation was calculated, and the calculation results for each model are shown in Table 5 and were also compared with the experimental results (Williams et al., 2006). Due to the hull symmetry in the tests with zero angle of attack, the lateral force should also be zero. To ensure the accuracy of results, the force value in the lateral direction was also calculated. A value of approximately 10^{-4} N was obtained, which indicated the accuracy of results.

Yaw static test

To calculate the hydrodynamic coefficients, vehicle movements at –20 to +20 degrees of angles of attack were simulated for four models (L/D = 8.5, 9.5, 10.5, and 12.5) in 2-degree intervals with a speed of 2 m/s. The results were compared with the experimental results in terms of longitudinal force, lateral force, and yawing moment (Figures 15, 17, and 19) (Azarsina & Williams, 2010). At a permanent angle of attack, upon increasing the length-to-diameter ratio, the longitudinal force increased because of an increase in the AUV hull surface, which increased the total resistance. The longitudinal force graph was symmetric relative to the zero-degree angle in terms of drift angle due to the symmetry of the hull relative to the longitudinal axis of the vehicle. In other words, the longitudinal force of the vehicle relative to the drift angle was an even function, and the drift angle was equivalent to the dimensionless lateral speed. The lateral force graph in terms of the drift angle was an odd function, i.e., the rotation direction of the vehicle affected the output force. At this stage, it was repeatedly observed that the lateral force increased at a permanent drift angle and increased length-to-diameter ratio. The yawing moment coefficient graph as a function of the angle of attack also produced an odd function (Figure 19).

The velocity distribution around the hull at a drift angle of 0° and a velocity of 2 m/s is shown in Figure 16, while Figure 18 shows the velocity distribution around the hull at a drift angle of 20° and a velocity of 2 m/s.

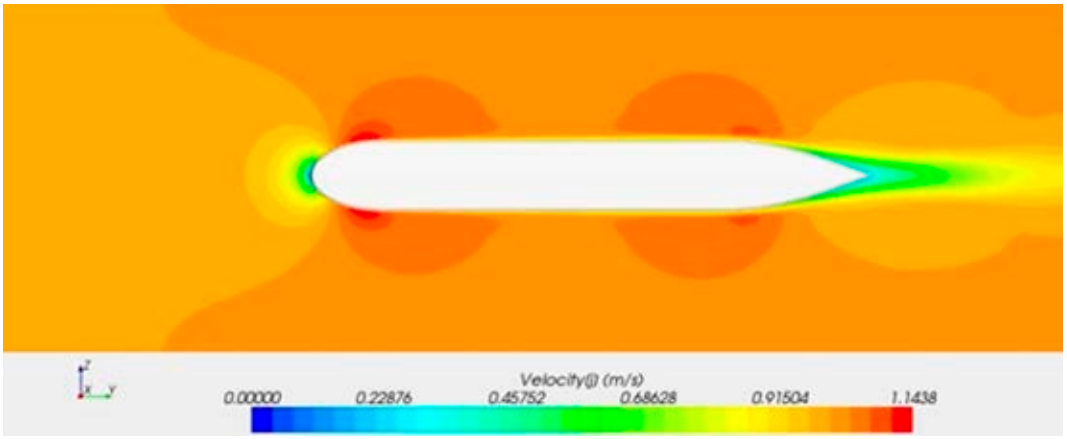

Figure 14. Velocity distribution around hull at 1 m/s velocity

Table 5. Resistance results with experimental and CFD

Model resistance LDR = 9.5 N			Model resistance LDR = 8.5 N			Model resistance LDR = 7.5 N			V m/s
Error %	CFD	EXP	Error %	CFD	EXP	Error %	CFD	EXP	
5.43	10.86	10.3	4.18	9.81	9.4	4.36	7.89	7.56	2
Model resistance LDR = 12.5 N			Model resistance LDR = 11.5 N			Model resistance LDR = 10.5 N			
5.17	12.3	11.6	3.84	11.63	11.2	3.49	10.97	10.6	2

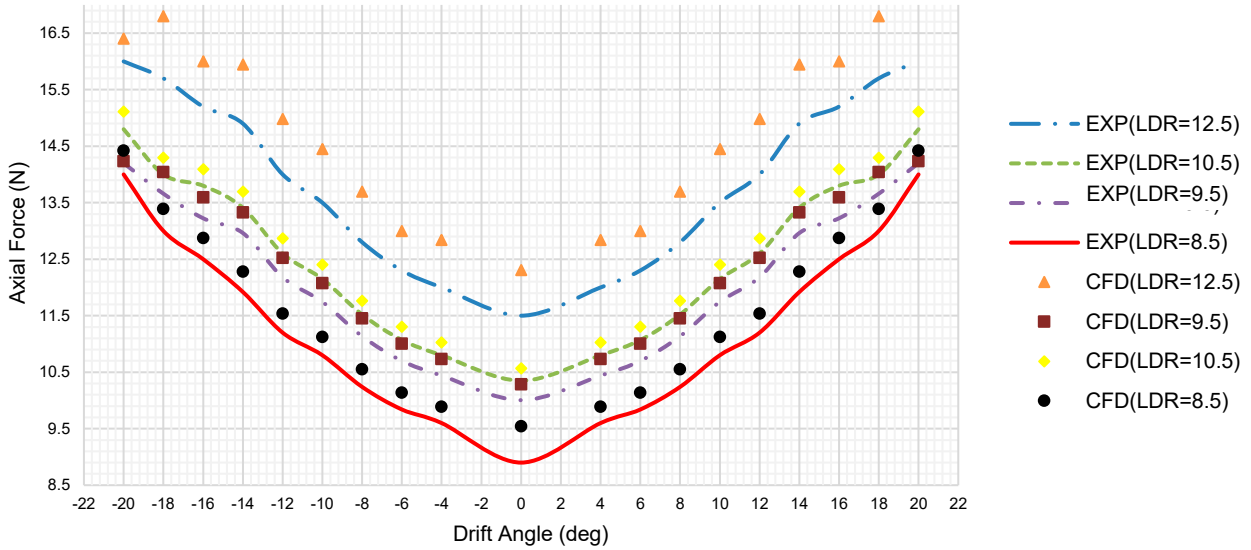

Figure 15. Axial force versus drift angle (V = 2 m/s)

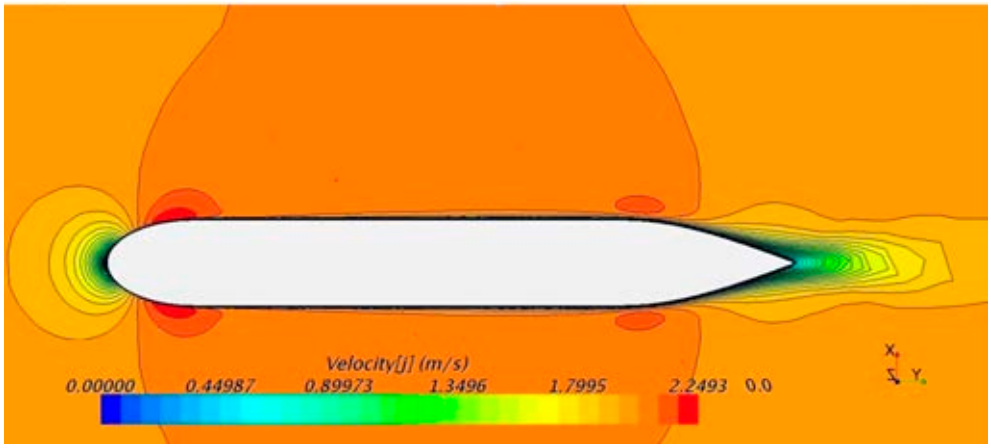

Figure 16. Velocity distribution around the hull (drift angle = 0°, V = 2 m/s)

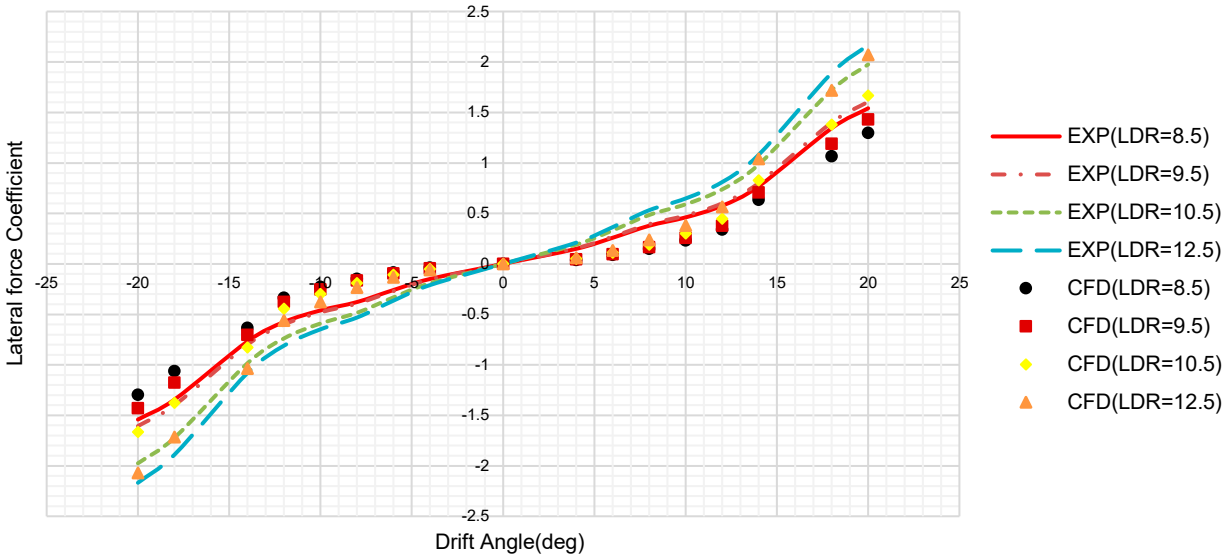

Figure 17. Lateral force coefficient versus drift angle (V = 2 m/s)

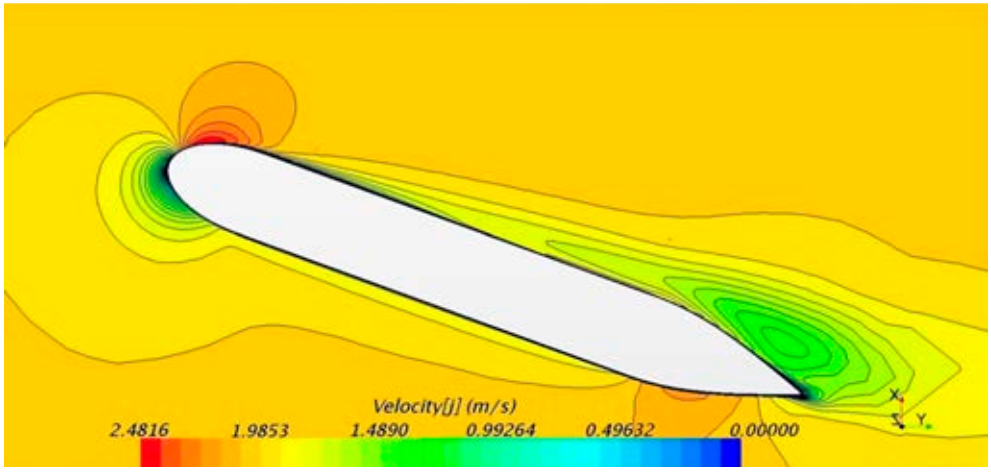

Figure 18. Velocity distribution around the hull (drift angle = 20°, V = 2m/s)

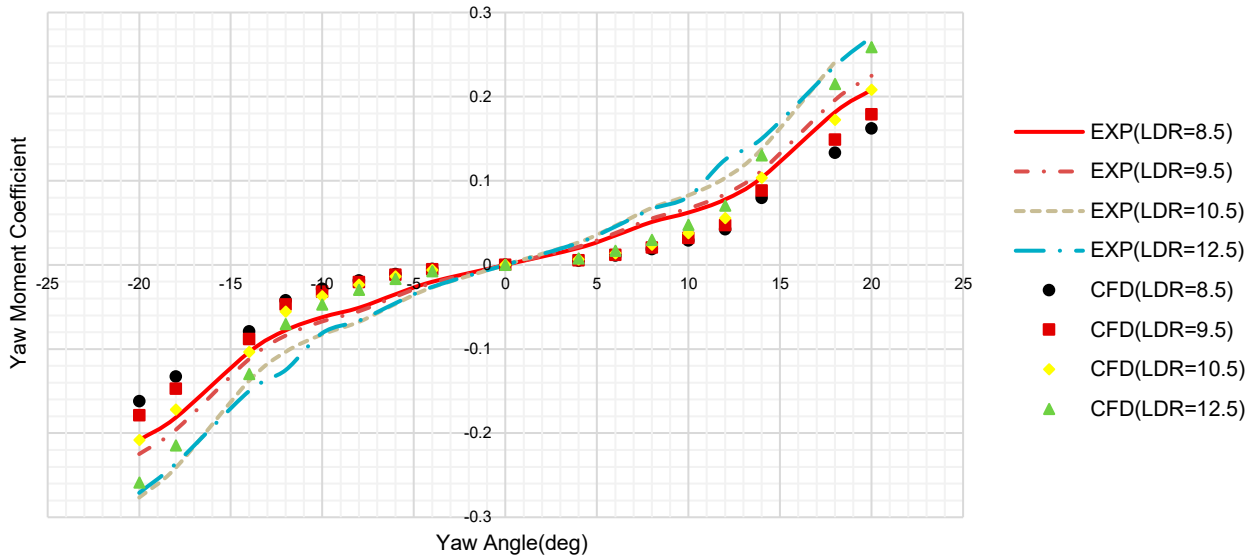

Figure 19. Yaw moment coefficient versus drift angle (V = 2 m/s)

Hydrodynamic coefficient calculations

With respect to the axial force results, the lateral force coefficient, lateral moment coefficients at drift angles from –20° to +20°, the dimensionless lateral force, or the lateral force can be calculated using the drag and lift coefficients:

$$Y' = C_D \sin\alpha + C_L \cos\alpha \tag{21}$$

where C_L and C_D are the lift and drag coefficients, respectively, and α is the angle of attack or drift angle. The dimensionless moment is equal to the yaw moment. To calculate the hydrodynamic coefficients for the calculated force and moment, a third-order model should be defined as follows:

$$Y' = Y'_v \cdot v' + Y'_{vvv} \cdot v'^3 \tag{22}$$

$$N' = N'_v \cdot v' + N'_{vvv} \cdot v'^3 \tag{23}$$

where $v' = \sin\alpha$. Unlike many methods, this does not have the problem of an acute angle of attack approximation; therefore, it is acceptable for v' to be a greater value. Table 6 shows the hydrodynamic coefficients of AUVs with different L/D. Using curve processing for the data, Y'_v, Y'_{vv}, N'_v and N'_{vv} coefficients can be calculated (Table 6).

Table 6. Hydrodynamic coefficients

L/D	Y'_v	Y'_{vvv}	N'_v	N'_{vvv}
8.5	0.0127	0.000006	0.044	0.00003
9.5	0.0142	0.00006	0.0539	0.00002
10.5	0.0157	0.00007	0.0563	0.00004
12.5	0.0185	0.000018	0.0679	0.0005

Conclusions

Maneuverability is an important hydrodynamic quality of a marine vehicle and should be predicted during the various design stages. There are various models to predict the manoeuvring properties of a marine vehicle, the most popular of which is the Abkowitz model, in which the external forces and moments are defined using hydrodynamic derivatives or coefficients. These hydrodynamic coefficients should be found in advance to predict the manoeuvring properties of a marine vehicle.

The computations were validated with experimental tests performed in the towing tank of the Isfahan University of Technology. The comparisons of the measured resistances and the computational results indicated that the CFD computations were reliable. OTT simulations were performed over a wide range of drift angles to compute the transverse velocity-dependent coefficients. All linear and nonlinear coefficients were obtained using the time mean of hydrodynamic forces, and the moments were calculated using CFD simulations. The coefficients were obtained using suitable curve fittings.

In the first section of this study, a new method was proposed for hydrodynamic simulations using CFD with the aid of CD-adapco software. Hydrodynamic forces and coefficients were calculated for different AUV models at different speeds. In the initial design stages, this method can be used to predict the manoeuvrability of an AUV and to design control systems for these AUVs. Another characteristic of this method was its ability to calculate non-linear hydrodynamic coefficients, which are essential for the application of non-linear manoeuvre models. Finally, the non-linear damping coefficients were calculated in the horizontal plane.

References

1. Azarsina, F. & Williams, C.D. (2010) Manoeuvring simulation of the MUN Explorer AUV based on the empirical hydrodynamics of axi-symmetric bare hulls. *Applied Ocean Research* 32 (4), pp. 443–453.
2. Azarsina, F., Williams, C. & Issac, M. (2008) Modelling the hydrodynamic sway force exerted on the bare-hull of an axi-symmetric underwater vehicle in lateral acceleration manoeuvres. *OCEANS 2008, IEEE*.
3. Blidberg, D.R. (2001) The development of autonomous underwater vehicles (AUV); a brief summary. *ICRA, IEEE*.
4. Dantas, J.L.D. & de Barros, E.A. (2013) Numerical analysis of control surface effects on AUV manoeuvrability. *Applied Ocean Research* 42, pp. 168–181.
5. Fan, S.-B., Lian, L., Ren, P. & Huang, G.-L. (2012) Oblique towing test and maneuver simulation at low speed and large drift angle for deep sea open-framed remotely operated vehicle. *Journal of Hydrodynamics, Ser. B* 24 (2), pp. 280–286.
6. Ferziger, J.H., Peric, M. & Leonard, A. (1997) *Computational methods for fluid dynamics*. AIP.
7. Gao, T., Wang, Y., Pang, Y. & Cao, J. (2016) Hull shape optimization for autonomous underwater vehicles using CFD. *Engineering Applications of Computational Fluid Mechanics* 10 (1), pp. 599–607.
8. Gentaz, L., Guillerm, P.E., Alessandrini, B. & Delhommeau, G. (1999) Three-dimensional free surface viscous flow around a ship in forced motion. *7th International Conference on Numerical Ship Hydrodynamics*.
9. Kim, Y.-G., Kim, S.-Y., Kim, H.-T., Lee, S.-W. & Yu, B.-S. (2007) Prediction of the maneuverability of a large container ship with twin propellers and twin rudders. *Journal of Marine Science and Technology* 12 (3), pp. 130–138.
10. Li, G. & Duan, W.-Y. (2011) Experimental study on the hydrodynamic property of a complex submersible. *Journal of Ship Mechanics* 15 (1–2), pp. 58–65.
11. Myring, D.F. (1976) A theoretical study of body drag in sub-critical axisymmetric flow. *Aeronautical Quarterly* 27 (3), pp. 186–194.
12. Nazir, Z., Su, Y.-M. & Wang, Z.-L. (2010) A CFD based investigation of the unsteady hydrodynamic coefficients of 3-D fins in viscous flow. *Journal of Marine Science and Application* 9 (3), pp. 250–255.
13. Obreja, D., Nabergoj, R., Crudu, L. & Păcuraru-Popoiu, S. (2010) Identification of hydrodynamic coefficients for manoeuvring simulation model of a fishing vessel. *Ocean Engineering* 37 (8), pp. 678–687.
14. Pan, Y.-C., Zhang, H.-X. & Zhou, Q.-D. (2012) Numerical prediction of submarine hydrodynamic coefficients using CFD simulation. *Journal of Hydrodynamics, Ser. B* 24 (6), pp. 840–847.
15. Ray, A., Singh, S. & Seshadri, V. (2009) Evaluation of linear and nonlinear hydrodynamic coefficients of underwater vehicles using CFD. *ASME 2009 28th International Conference on Ocean, Offshore and Arctic Engineering*, American Society of Mechanical Engineers.
16. Roache, P.J. (1997) Quantification of uncertainty in computational fluid dynamics. *Annual Review of Fluid Mechanics* 29 (1), pp. 123–160.
17. Sarkar, T., Sayer, P. & Fraser, S. (1997) A study of autonomous underwater vehicle hull forms using computational fluid dynamics. *International Journal for Numerical Methods in Fluids* 25 (11), pp. 1301–1313.
18. Tyagi, A. & Sen, D. (2006). Calculation of transverse hydrodynamic coefficients using computational fluid dynamic approach. *Ocean Engineering* 33 (5), pp. 798–809.
19. Williams, C., Curtis, T., Doucet, J., Issac, M. & Azarsina, F. (2006) Effects of hull length on the hydrodynamic loads on a slender underwater vehicle during manoeuvres. *OCEANS 2006, IEEE*.
20. Wilson, R., Paterson, E. & Stern, F. (1998) Unsteady RANS CFD method for naval combatant in waves. In Proceedings of the 22nd Symposium on Naval Hydrodynamics, Washington, D.C., pp. 532–549.